

Zahra S. Hosseini

Department of Mechanical Science and Engineering,
University of Illinois at Urbana-Champaign,
Urbana, IL 61801;
International Institute for Carbon-Neutral Energy
Research (WPI-I2CNER),
Kyushu University,
Fukuoka 819-0395, Japan
e-mail: hssnsm2@illinois.edu

Mohsen Dadfarnia

Department of Mechanical Engineering,
Seattle University,
901 12th Street,
Seattle, WA 98122;
International Institute for Carbon-Neutral Energy
Research (WPI-I2CNER),
Kyushu University,
Fukuoka 819-0395, Japan
e-mail: dadfarniamoh@seattleu.edu

Akihide Nagao

International Institute for Carbon-Neutral Energy
Research (WPI-I2CNER),
Kyushu University,
Fukuoka 819-0395, Japan
e-mail: akihidenagao@gmail.com

Masanobu Kubota

International Institute for Carbon-Neutral Energy
Research (WPI-I2CNER),
Kyushu University,
Fukuoka 819-0395, Japan
e-mail: kubota.masanobu.304@m.kyushu-u.ac.jp

Brian P. Somerday

Department of Mechanical Science and Engineering,
University of Illinois at Urbana-Champaign,
Urbana, IL 61801;
International Institute for Carbon-Neutral Energy
Research (WPI-I2CNER),
Kyushu University,
Fukuoka 819-0395, Japan
e-mail: bpsomer@illinois.edu

Robert O. Ritchie

Materials Sciences Division, Lawrence Berkeley
National Laboratory, and Department of Materials
Science and Engineering,
University of California, Berkeley,
Berkeley, CA 94720;
International Institute for Carbon-Neutral Energy
Research (WPI-I2CNER),
Kyushu University,
Fukuoka 819-0395, Japan
e-mail: roritche@lbl.gov

Modeling the Hydrogen Effect on the Constitutive Response of a Low Carbon Steel in Cyclic Loading

Hydrogen-accelerated fatigue crack growth is a most severe manifestation of hydrogen embrittlement. A mechanistic and predictive model is still lacking partly due to the lack of a descriptive constitutive model of the hydrogen/material interaction at the macroscale under cyclic loading. Such a model could be used to assess the nature of the stress and strain fields in the neighborhood of a crack, a development that could potentially lead to the association of these fields with proper macroscopic parameters. Toward this goal, a constitutive model for cyclic response should be capable of capturing hardening or softening under cyclic straining or ratcheting under stress-controlled testing. In this work, we attempt a constitutive description by using data from uniaxial strain-controlled cyclic loading and stress-controlled ratcheting tests with a low carbon steel, Japanese Industrial Standard (JIS) SM490YB, conducted in air and 1 MPa H₂ gas environment at room temperature. We explore the Chaboche constitutive model which is a nonlinear kinematic hardening model that was developed as an extension to the Frederick and Armstrong model, and propose an approach to calibrate the parameters involved. From the combined experimental data and the calibrated Chaboche model, we may conclude that hydrogen decreases the yield stress and the amount of cyclic hardening. On the other hand, hydrogen increases ratcheting, the rate of cyclic hardening, and promotes stronger recovery.
[DOI: 10.1115/1.4049076]

Keywords: fatigue, hydrogen embrittlement

¹Corresponding author.

Contributed by the Applied Mechanics Division of ASME for publication in the JOURNAL OF APPLIED MECHANICS. Manuscript received August 27, 2020; final manuscript received November 6, 2020; published online December 4, 2020. Assoc. Editor: Noy Cohen.

1 Introduction

Materials loaded in the presence of hydrogen experience mechanical degradation which can be demonstrated as reduced elongation and reduction in area, decreased fracture toughness, accelerated fatigue crack growth, and shortened cyclic fatigue life [1–12]. Such hydrogen-induced degradation of mechanical properties is usually accompanied by transition of deformation processes and fractography [1–12].

Under monotonically increasing or sustained loading [13–21], the hydrogen effect has been investigated extensively and the fundamental hydrogen embrittlement phenomenology has been fairly well analyzed from detailed microstructural observations [18,19], fractographic studies [15], and mechanistic models [13,14,16]. The hydrogen effect on fatigue life and the associated microstructural characteristics of fracture have been investigated under uniaxial cyclic loading [10,22–27]. Investigating the response of an annealed medium carbon steel under uniaxial stress-controlled loading, Uyama et al. [22] observed that hydrogen decreases the strain range under a given stress amplitude while it has no effect on fatigue life. On the other hand, Tsuchida et al. [23] carrying out strain-controlled tests with a low carbon S10 ferritic-pearlitic steel under cathodic charging observed that the fatigue life decreases in the presence of hydrogen. Such fatigue life decrease in hydrogen was also observed in other studies [10,24–26]. Martin et al. [25] investigated the fatigue life of a 4130 steel under uniaxial strain-controlled cyclic loading in an effort to develop “accurate fracture mechanics modeling” of fatigue in the presence of hydrogen. They observed that the fatigue life in air is approximately two orders of magnitude longer than in 18 MPa hydrogen. Martin et al. [25] also used the cyclic stress–strain response to fit the Morrow damage model [28]. Das and Singh [26] investigated the effect of hydrogen on P91 steel under strain-controlled cyclic loading. Using the cyclic stress–strain data to fit the Masing model curve, they concluded that the strength of the hydrogen-charged specimen is lower than that of the uncharged. Notably, Das and Singh [26] used the stress–strain data from a single cycle with strain amplitude of 1% to calibrate the Chaboche model for the material constitutive response. However, on the basis of the reported calibrated parameters, it seems that only the first kinematic hardening rule was treated as affected by hydrogen while the second and third kinematic hardening rules were considered to be the same in the hydrogen-charged and uncharged material. Das and Singh [26] also observed cyclic softening in both hydrogen-charged and uncharged specimens with the rate of softening being higher in the presence of hydrogen. Similar hydrogen effect on the rate of cyclic softening was also reported by Mansilla et al. [27] for high strength steel. In summary, with the exception of the work of the Das and Singh [26], the above studies, while they address the hydrogen effect on fatigue life in uniaxial cycling loading, do not provide a framework for the development of a constitutive model that can be used to quantify the local stress and strain fields under cycling loading in the presence of hydrogen.

Despite the fact that hydrogen-induced fatigue crack growth data as well as relevant metallographic [3,4] and fractographic results [1,11,12] have become available for a number of metals and alloys, the salient mechanisms responsible for hydrogen-accelerated fatigue crack growth [1,9,11,12,20] still remain poorly understood, in part because of the complexities inherent in the growth of fatigue cracks. This lack of mechanistic understanding and hydrogen-informed constitutive models limited the field of fatigue crack growth modeling to mainly phenomenological approaches as in cases involving modification of the Paris law parameters or the use of von Mises plasticity with Ramberg-Osgood hardening. It is worth noting that the classical von Mises plasticity model with associated flow rule fails to address such features of the cyclic response as hardening/softening or ratcheting [29].

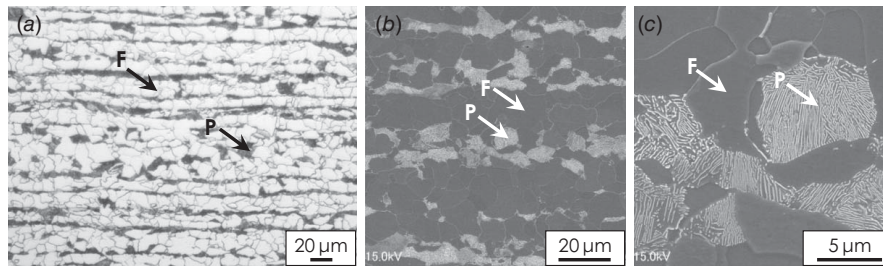
Given the lack of predictive mechanistic models for hydrogen-accelerated fatigue crack growth, the development of a well characterized constitutive law is essential to quantifying local stress and strain fields under cyclic loading relative to macroscopically measured parameters. We note that full characterization of the stress and strain fields at a crack tip have been the landmark breakthroughs that enabled the successful development of the linear elastic and elastoplastic fracture mechanics, and we view such characterization to be of the same importance in the case of fatigue in the presence of hydrogen. As two noted researchers in the field of mechanics of materials [30] emphasized “Fracture mechanics is the judicious interpretation of stress and strain field ahead of the crack tip.” In this context, the objective of this work is to present precisely an approach for the development of a proper constitutive model specifically for material response under cycling loading.

Most metals and alloys subjected to strain-controlled cyclic loading exhibit either cyclic hardening or cyclic softening with subsequent stabilization after a certain number of cycles [28,31]. In a three-dimensional setting, this can be interpreted in terms of a stabilized yield surface after a certain number of cycles. Another cyclic loading feature is ratcheting under stress-controlled testing with nonzero mean stress. It has been shown that material models formulated with nonlinear kinematic hardening rules exhibit ratcheting response [32,33]. In these models, the stabilization of the yield surface is addressed by adding an isotropic hardening/softening increment to the flow stress. Seminal in this area is the nonlinear kinematic hardening model developed by Armstrong and Frederick [34]. Subsequent to this work, several models were proposed based on Armstrong and Frederick’s approach to improve the capability to predict ratcheting [32,33,35–41]. Notable among these revised approaches was that of Chaboche and Nouailhas [33]. The model is capable of capturing many prominent features induced by cyclic loading such as plastic shakedown, ratcheting, and the relaxation of the mean stress.

The present work is a combined experimental and theoretical attempt to explore and model the hydrogen effect on the constitutive response of materials subjected to cyclic loading. To accomplish this, we rely on the Chaboche constitutive model which we calibrate

Table 1 Chemical composition (mass%) of JIS SM490YB steel

Steel	C	Si	Mn	P	S	Cr	Nb	Al soluble	Total N	O
JIS SM490YB	0.155	0.27	1.41	0.015	0.0030	0.03	0.008	0.031	0.0020	0.0013

**Fig. 1 Microstructure of JIS SM490YB steel: (a) optical image, Nital etched; (b) and (c) SEM images, Nital etched. F and P indicate ferrite and pearlite, respectively.**

using a sequence of experimental data from uniaxial strain-controlled cyclic loading tests and uniaxial stress-controlled ratcheting tests with a low carbon steel, Japanese Industrial Standard (JIS) SM490YB, in the absence and presence of hydrogen.

2 Experiment

2.1 Material. The material used in this study was the JIS G 3106 (2015) Grade SM490YB steel, which is a low carbon rolled steel used for welded structures. The chemical composition is shown in Table 1. A small amount of Nb was added to refine the grains. A slab was reheated to austenite phase and was hot rolled into a steel plate shape of thickness of 16 mm.

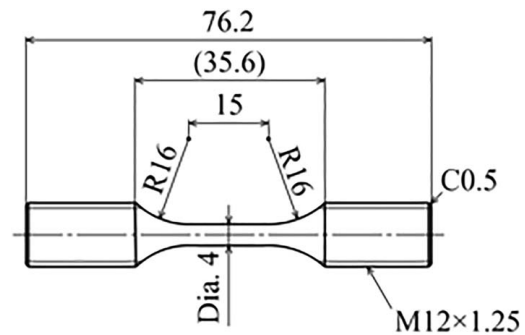
The surface of the sample was etched with 3% Nital to reveal the microstructure for the optical microscopy and scanning electron microscopy (SEM) studies. A Hitachi S-4000 field-emission scanning electron microscope operating at an accelerating voltage of 15 kV was used for the examination of the microstructure. The microstructure of the steel at the quarter section of the steel plate and perpendicular to the rolling direction is shown in Fig. 1. It exhibits a mixed ferrite and pearlite colony microstructure with ferrite mean grain size of $\sim 15 \mu\text{m}$ and pearlite volume fraction of $\sim 25\%$. The pearlite was formed in steak-like bundles along the rolling direction, which suggests that the austenite phase was first transformed into ferrite phase in bundles along the rolling direction during cooling after hot rolling and then the remainder of the austenite with a higher carbon concentration was transformed into the pearlite phase.

The tensile properties of the steel in the absence of hydrogen are summarized in Table 2. The tensile specimens were machined on a lathe from the steel plate, with the center of the specimens at the middle thickness portion of the plate and perpendicular to the rolling direction. The stress-strain curve showed clear yielding behavior with an ultimate tensile strength of 552 MPa. Further, the hardness distribution along the thickness of the plate, as determined using a standard 98.1 N Vickers indent, exhibited a bowl shape, *i.e.*, lowest at the middle portion of the plate ($\text{HV}_{10} = 144$) and highest at the surface portion ($\text{HV}_{10} = 156$). This reflects the distribution of microstructure along the thickness of the plate with the surface section having the most refined grains.

2.2 Strain- and Stress-Controlled Fatigue Tests. A schematic illustration of the specimen used for strain- and stress-controlled fatigue tests is shown in Fig. 2. The specimen is a cylindrical bar and the diameter and the gauge length of the reduced section are 4.0 and 15 mm, respectively. From previous studies

Table 2 Mechanical properties of JIS SM490YB steel

Steel	Lower yield strength σ_Y (MPa)	Ultimate tensile strength σ_B (MPa)	Total elongation δ (%)	Reduction in area φ (%)
JIS SM490YB	411	552	32.8	74.5

**Fig. 2 Schematic of the specimen used for the strain- and stress-controlled fatigue tests. Dimensions are in millimeters.**

[42] on hydrogen uptake in steels exposed to gaseous hydrogen, it is known that natural oxide film covering the specimen surface prevents hydrogen uptake. Moreover, Pd plating accelerates hydrogen uptake in steels by transitioning its endothermic reaction into exothermic reaction as well as by lowering both the hydrogen adsorption and absorption energies that represent the energy barriers from the physisorption state to the chemisorption state and from the chemisorption state to the sub-surface state, respectively [42,43]. Hence, all the specimens charged with hydrogen were electroplated with Pd of $\sim 74 \text{ nm}$ thickness.

The experimental apparatus for the strain- and stress-controlled fatigue tests is shown in Fig. 3. These fatigue tests were carried out under tension and compression loading both in air and 1 MPa hydrogen gas. For the strain-controlled fatigue tests, strain was measured by a strain-gauge type extensometer. The strain rate was controlled at $1.3 \times 10^{-3} / \text{s}$. Failure of the specimen was identified with a 25% reduction of the maximum stress from the initial maximum stress. The stress-controlled fatigue tests were conducted under

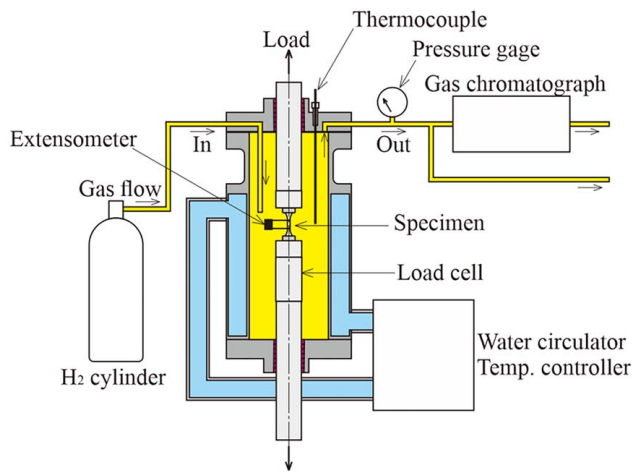


Fig. 3 Fatigue testing machine apparatus with a gas chamber

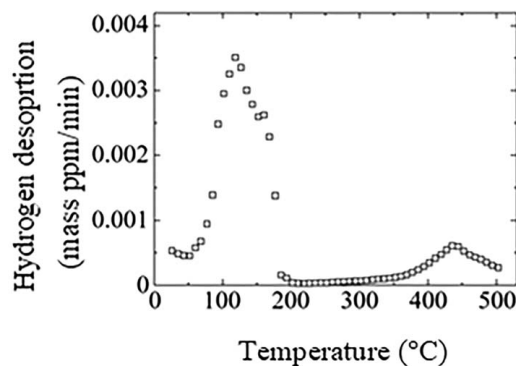


Fig. 4 Thermal desorption analysis spectrum of the Pd-plated specimen exposed to 1 MPa hydrogen gas for 24 h without loading. The rate of heating is 100 °C/h.

load control with a constant stress amplitude and two levels of mean stress. The stress amplitude and mean stress were selected so that the maximum stress was sufficiently higher than the yield stress and ratcheting behavior was observed. The stress amplitude $\sigma_a = (\sigma_{\max} - \sigma_{\min})/2$ was 420 MPa, where σ_{\max} and σ_{\min} are maximum and minimum stress, respectively. The values of the mean stress $\sigma_{\text{mean}} = (\sigma_{\max} + \sigma_{\min})/2$ were 20 and 40 MPa.

The atmospheric temperature of air and hydrogen gas was controlled at 20 °C. The tests in hydrogen were started 24 h after the 1 MPa hydrogen gas environment was established in order for a uniform hydrogen distribution throughout the specimen diameter prior to testing be established. Calculation of the transient hydrogen distribution throughout the cylindrical part of the gauge section [44] yields a saturation time equal to $Dt/a^2 = 1.0$ which implies that a uniform hydrogen distribution was established throughout the specimen in 1.1 h for $D = 10^{-9} \text{ m}^2/\text{s}$ [45] and radius $a = 2.0 \text{ mm}$.

A thermal desorption analysis spectrum from the Pd-plated specimen that was exposed to 1 MPa hydrogen gas for 24 h with no loading is presented in Fig. 4. The sample was heated at a constant rate of 100 °C/h from room temperature to 500 °C to evolve the hydrogen in a controlled manner. The hydrogen-charged sample shows two broad peaks with prominent desorption peak rates at 120 and 440 °C. The first peak that appears in the thermal desorption analysis spectrum is defined as peak 1 hydrogen associated with hydrogen atoms trapped at low energy traps such as dislocations and ferrite/cementite interfaces in the pearlite colonies [19,46]. The peak 1 hydrogen content in Fig. 4 was 0.16 mass ppm. The peak 2 hydrogen content was much smaller than the associated with the peak 1 and corresponds to hydrogen trapped at higher energy traps such as grain boundaries [19].

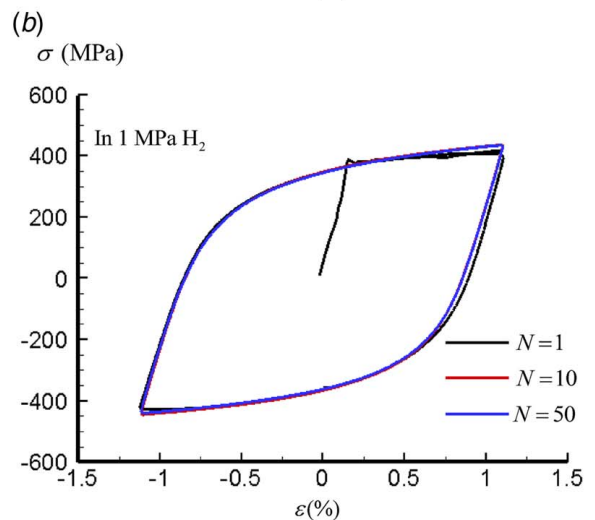
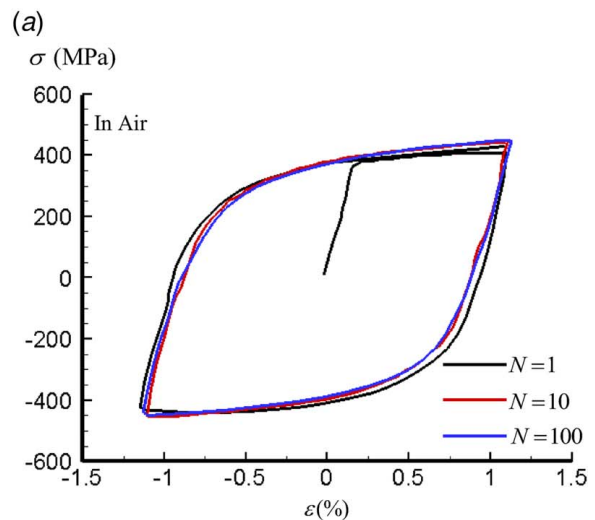


Fig. 5 Stress–strain curves for uniaxial strain-controlled tests with strain range $\Delta\varepsilon = 2.2\%$: (a) in air at cycles $N = 1, 10,$ and 100 and (b) in 1 MPa hydrogen gas at cycles $N = 1, 10,$ and 50

2.2.1 Strain- and Stress-Controlled Fatigue Test Results. The strain-controlled fatigue tests were carried out for strain ranges $\Delta\varepsilon$ of 0.92%, 1.08%, and 2.2%. Figures 5–7 show the results in air and 1 MPa hydrogen gas. The stable cyclic stress–strain curves are shown in Fig. 8. The hysteresis loops in the absence of hydrogen show that the steel is hardened for $\Delta\varepsilon = 2.2\%$ and softened for 0.92% and 1.08% (please see relevant discussion in Sec. 5). Figure 9 shows the number of cycles to failure as a function of strain range $\Delta\varepsilon$ in air and 1 MPa hydrogen gas. Clearly, the fatigue life in hydrogen gas is shorter than that in air. Such effect of hydrogen on the fatigue life was also observed in other experimental studies [10,23–26].

Figure 10 shows ratcheting data in air and 1 MPa hydrogen gas at mean stresses σ_{mean} equal to 20 and 40 MPa. The maximum strain associated with the maximum stress σ_{\max} at any cycle, ε_{\max} , is higher in the presence of hydrogen for both values of σ_{mean} .

3 The Chaboche Constitutive Model for Cyclic Plasticity

As we mentioned in Sec. 1, we explored the Chaboche constitutive model [32,33,36,38] to describe the cyclic plasticity of JIS SM490YB steel, as this model is arguably the most promising in reproducing features of cyclic response. First, we briefly describe the model and its features, the idea being to associate these features

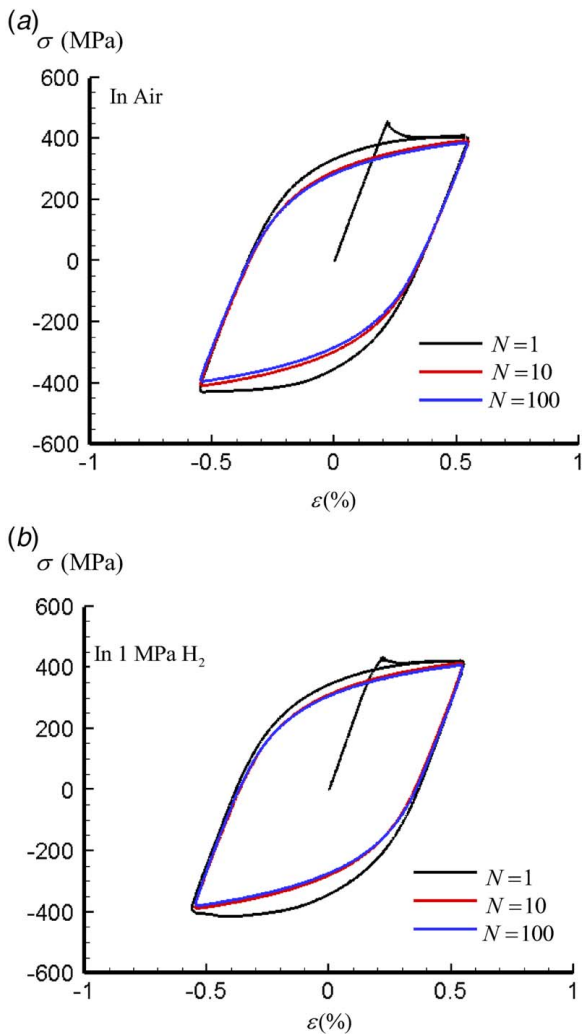


Fig. 6 Stress–strain curves for uniaxial strain-controlled tests with strain range $\Delta\varepsilon = 1.08\%$: (a) in air at cycle $N = 1, 10,$ and 100 and (b) in 1 MPa hydrogen gas at cycle $N = 1, 10,$ and 100

with the experimental response for subsequent calibration. In this regard, we also present the form of the model in uniaxial cycling loading.

3.1 Formulation. We assume that the deformation rate tensor \mathbf{D} is decomposed into elastic \mathbf{D}^e and plastic \mathbf{D}^p components [47]:

$$\mathbf{D} = \mathbf{D}^e + \mathbf{D}^p \quad (1)$$

For linear and isotropic elasticity:

$$\mathbf{D}^e = \frac{1}{2G} \overset{\nabla}{\boldsymbol{\sigma}} - \frac{\nu}{1 + \nu} \frac{1}{2G} \overset{\nabla}{\sigma_{kk}} \boldsymbol{\delta} \quad (2)$$

where $\overset{\nabla}{\boldsymbol{\sigma}}$ is the Jaumann derivative of the Cauchy stress tensor $\boldsymbol{\sigma}$, $\boldsymbol{\delta}$ is the second-order identity tensor whose components δ_{ij} are the Kronecker delta, and G, ν are, respectively, the shear modulus and Poisson's ratio. For isotropic yielding

$$f(\boldsymbol{\sigma}, \boldsymbol{\alpha}, R) = \Sigma_e - \sigma_0 - R = 0 \quad (3)$$

where $\Sigma_e = \sqrt{(3/2)(\boldsymbol{\sigma}' - \boldsymbol{\alpha}) : (\boldsymbol{\sigma}' - \boldsymbol{\alpha})}$ is the effective stress, $\boldsymbol{\sigma}'$ is the deviatoric stress tensor, $\boldsymbol{\alpha}$ is the back stress tensor, σ_0 is the yield stress, and R describes either isotropic hardening if positive or

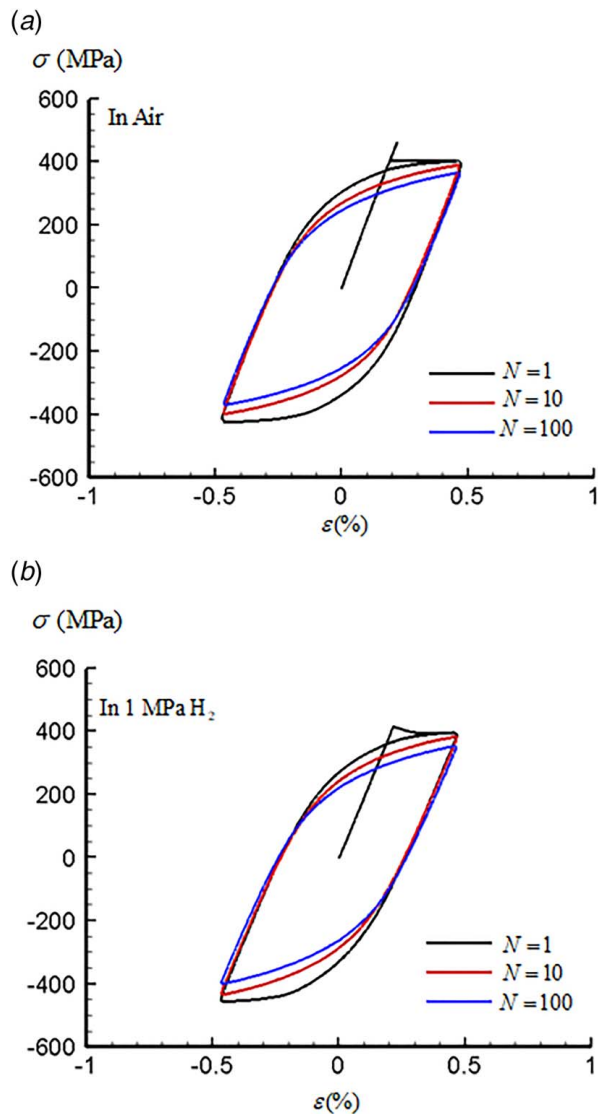


Fig. 7 Stress–strain curves for uniaxial strain-controlled tests with strain range $\Delta\varepsilon = 0.92\%$: (a) in air at cycle $N = 1, 10,$ and 100 and (b) in 1 MPa hydrogen gas at cycle $N = 1, 10,$ and 100

isotropic softening if negative, and it is the increment to the yield stress that modulates the stabilization of the response in strain-controlled cyclic loading.

The back stress tensor is composed of three parts, $\boldsymbol{\alpha} = \boldsymbol{\alpha}_1 + \boldsymbol{\alpha}_2 + \boldsymbol{\alpha}_3$, with corresponding time rate of change:

$$\overset{\nabla}{\boldsymbol{\alpha}}_i = \frac{2}{3} C_i \mathbf{D}^p - \gamma_i \boldsymbol{\alpha}_i \dot{\varepsilon}^p, \quad i = 1, 2, 3 \quad (\text{no summation over } i) \quad (4)$$

where C_i and γ_i are material constants

$$\dot{\varepsilon}^p = \sqrt{2 D_{ij}^p D_{ij}^p / 3} \quad (5)$$

is the effective plastic strain rate and the standard summation convention is implied over a repeated index. The associated flow rule leads to

$$\mathbf{D}^p = \dot{\varepsilon}^p \mathbf{N} \quad (6)$$

in which $\mathbf{N} = \partial f(\boldsymbol{\sigma}, \boldsymbol{\alpha}, R) / \partial \boldsymbol{\sigma} = 3(\boldsymbol{\sigma}' - \boldsymbol{\alpha}) / 2\Sigma_e$ is the normal to the yield surface and $\boldsymbol{\sigma}'$ is the stress deviator. The time rate

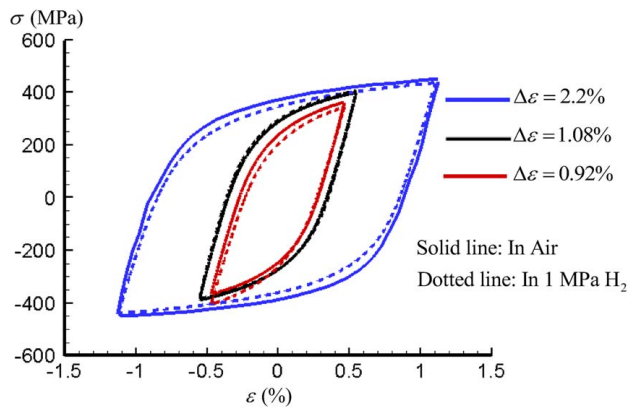


Fig. 8 Stable stress–strain hysteresis curves for uniaxial strain-controlled tests at strain ranges $\Delta\varepsilon = 0.92\%$, 1.08% , and 2.2% in air and 1 MPa hydrogen gas

of change of the isotropic hardening/softening parameter R is expressed as

$$\dot{R} = h(Q - R)\dot{\varepsilon}^p \quad (7)$$

where h and Q are constants. Integration of Eq. (7) yields

$$R = Q(1 - e^{-h\varepsilon^p}) \quad (8)$$

and Fig. 11 shows a schematic for the variation of R as a function of the accumulated plastic strain ε^p . R increases monotonically and levels to a value Q which is positive (negative) for cyclic hardening (softening). It is noted that the parameter Q determines the amount of cyclic hardening/softening during a strain-controlled test. In other words, the change in the maximum stress from the first cycle to the stabilized cycle is controlled by the parameter Q .

In summary, the Chaboche model for cyclic plasticity that we adopted in this work involves nine parameters: C_1 , C_2 , C_3 , γ_1 , γ_2 , γ_3 , Q , h , and σ_0 that can be calibrated experimentally. The calibration process is outlined in Sec. 4.

3.2 Uniaxial Strain-Controlled Cyclic Response. Our experimental results for the stabilized stress–strain hysteresis loop shown

in Fig. 12 for the case $\Delta\varepsilon = 2.2\%$ show three distinct segments [32,33,41]:

- (i) Segment 1: the part of the stable hysteresis curve with high modulus at the onset of yielding and very small plastic strains;
- (ii) Segment 2: the transient nonlinear portion of the hysteresis curve at moderate plastic strains;
- (iii) Segment 3: the subsequent part of the hysteresis curve that varies almost linearly with plastic strain at large plastic strains.

Recall that the Chaboche nonlinear kinematic hardening model [32,33] involves a superposition of three Armstrong and Frederick [34] hardening rules, i.e., $\alpha = \alpha_1 + \alpha_2 + \alpha_3$ with corresponding evolution rules given by Eq. (4). Each of the three hardening rules controls the behavior of a corresponding segment of the hysteresis loop. The first rule, α_1 , governs initial hardening with a large modulus at very small plastic strains (segment 1), the second rule, α_2 , governs the nonlinear behavior at moderate plastic strains (segment 2), and the third hardening rule, α_3 , governs the nearly linear segment of the hysteresis loop along which the modulus is nearly constant (segment 3). The above three features of the Chaboche model will be further clarified in the discussion for the calibration of the model relative to Fig. 13 in Sec. 4.

First, we consider the uniaxial strain-controlled response under fully reversed tension/compression cyclic loading, i.e., $\varepsilon_{\max}^p = -\varepsilon_{\min}^p$. As shown in Appendix A, the closed form solution for the stable hysteresis loop is given by

$$\sigma_{xx} = \frac{C_1}{\gamma_1} (1 - 2 \exp(-\lambda\gamma_1(\varepsilon^p - \lambda\varepsilon_{\min}^p))) + \frac{C_2}{\gamma_2} (1 - 2 \exp(-\lambda\gamma_2(\varepsilon^p - \lambda\varepsilon_{\min}^p))) + C_3\varepsilon^p + \lambda\sigma_0 + \lambda Q \quad (9)$$

where σ_{xx} is the axial stress. As can be seen from Eq. (9), the parameter γ_3 does not appear in the solution for the stabilized loop because of its absence from the third hardening rule; see Appendix A for relevant details.

The maximum stress σ_{MS} in the stable hysteresis loop is obtained from Eq. (9) for $\varepsilon^p = \varepsilon_{\max}^p$ and $\lambda = 1$:

$$\sigma_{MS} = \alpha_{MS} + \sigma_0 + Q \quad (10)$$

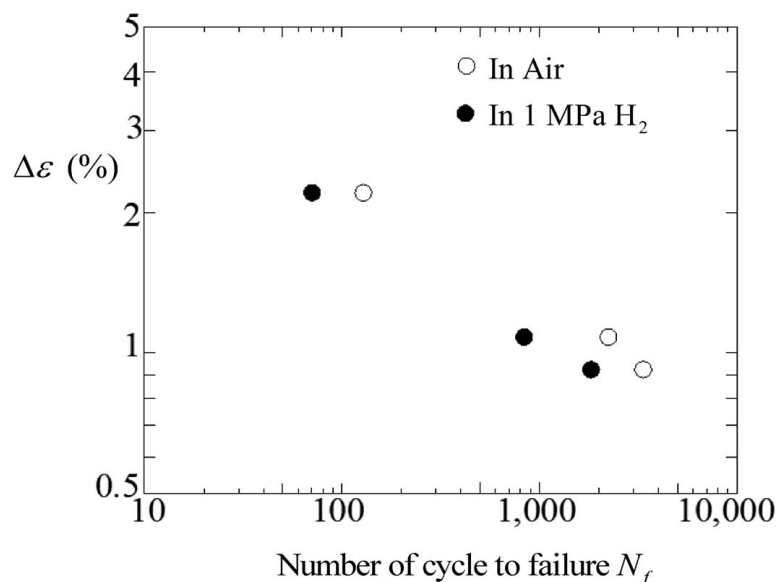


Fig. 9 Fatigue life determined from the strain-controlled fatigue tests in air and 1 MPa hydrogen gas as a function of strain range $\Delta\varepsilon$

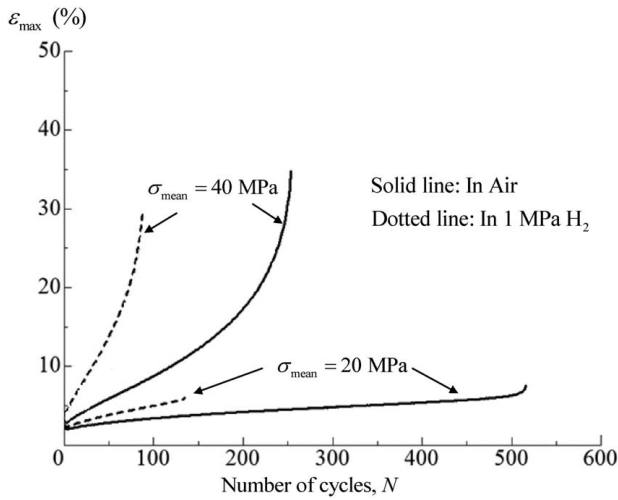


Fig. 10 Ratcheting data from uniaxial stress-controlled tests with stress amplitude $\sigma_a = 420$ MPa and mean stress $\sigma_{\text{mean}} = 20$ and 40 MPa in air and 1 MPa hydrogen gas

where α_{MS} is the maximum back stress in the stable cycle given by

$$\alpha_{MS} = \frac{C_1}{\gamma_1} + \frac{C_2}{\gamma_2} + C_3 \varepsilon_{\text{max}}^p \quad (11)$$

under the assumption that the parameters γ_i ($i = 1, 2$) are large so that $\exp(-\gamma_i \Delta \varepsilon^p) \sim 0$, as discussed in Appendix A.

4 Calibration

In this section, we present our approach to determining the nine parameters of the Chaboche model by using:

- The results from the uniaxial strain-controlled tests for the three different strain ranges $\Delta \varepsilon = 0.92\%$, 1.08% , and 2.2% along with Eq. (9) to determine the parameters C_1 , C_2 , C_3 , γ_1 , γ_2 , Q , h , and σ_0 .
- The results from the stress-controlled ratcheting tests with stress amplitude 420 MPa and mean stresses 20 MPa and 40 MPa to determine the remaining parameter γ_3 .

4.1 Determination of Parameters C_1 , C_2 , C_3 , γ_1 , γ_2 , Q , and σ_0 in the Absence of Hydrogen. As can be observed from Fig. 8, the effect of hydrogen on the response of SM490YB steel can only be discerned for $\Delta \varepsilon = 2.2\%$ in comparison with $\Delta \varepsilon = 0.92\%$ and 1.08% . Hence, for the calibration, we use the stable stress–strain hysteresis loop data for $\Delta \varepsilon = 2.2\%$ as plotted in Fig. 12 in the absence of hydrogen. By construction of the Chaboche model, the slope of segment 1 is controlled by the first hardening rule. Hence by neglecting the contributions of C_2 and C_3 to the slope of the hysteresis curve at small strains, we have $d\sigma_{xx}/d\varepsilon^p \sim 2C_1$ at $\varepsilon^p = \varepsilon_{\text{min}}^p$, which along with Fig. 12 yields

$$C_1 = 3.2 \times 10^5 \text{ MPa} \quad (12)$$

Again, by construction of the Chaboche model, the slope of segment 3 is controlled by the parameter C_3 , which is warranted if the parameters γ_i ($i = 1, 2$) are large so that $\exp(-\gamma_i \Delta \varepsilon^p) \sim 0$. Thus, $d\sigma_{xx}/d\varepsilon^p \sim C_3$ at $\varepsilon^p = \varepsilon_{\text{max}}^p$ and along with Fig. 12 we find

$$C_3 = 5.3 \times 10^3 \text{ MPa} \quad (13)$$

In order to determine the parameter Q , we use Eq. (A3) to obtain the maximum stress in cycle N

$$\sigma_{MN} = \alpha_{MN} + \sigma_0 + R_N \quad (14)$$

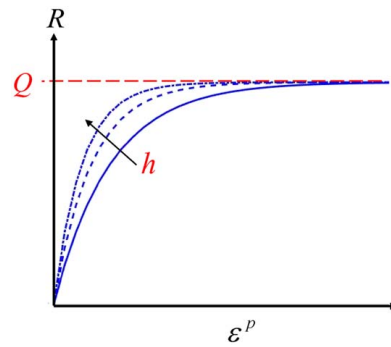


Fig. 11 Evolution of the isotropic hardening parameter R with plastic strain ε^p . The parameters h and Q control the rate of evolution and the maximum values (see Eq. (8)).

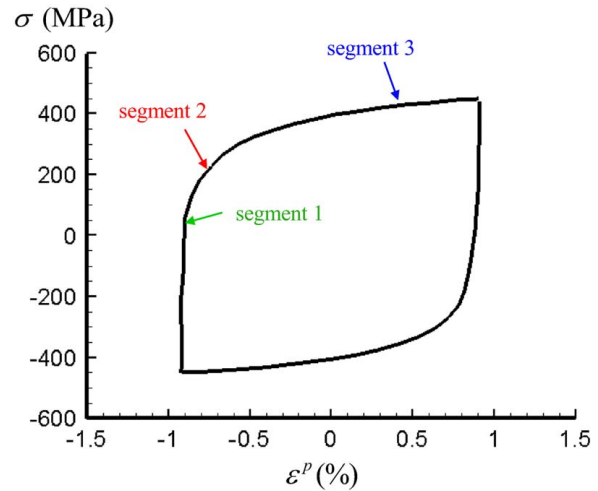


Fig. 12 Experimentally measured stable stress–strain hysteresis loop for SM490YB steel under uniaxial strain-controlled cyclic loading with strain range $\Delta \varepsilon = 2.2\%$ in air. The stress is plotted against plastic strain ε^p whose range $\Delta \varepsilon^p$ is about 2%.

where σ_{MN} , α_{MN} , and R_N are, respectively, the maximum stress, maximum back stress, and the isotropic hardening parameter R associated with the cycle N for $\varepsilon^p = \varepsilon_{\text{max}}^p$. Using Eqs. (10) and (14) along with $\alpha_{M1} = \alpha_{MS}$,² one finds

$$\sigma_{MS} - \sigma_{M1} = R_S - R_1 \quad (15)$$

where R_S and R_1 are, respectively, the values of the isotropic hardening parameter R associated with the stable cycle and the first cycle for $\varepsilon^p = \varepsilon_{\text{max}}^p$. Recalling that R levels to Q at stabilization, i.e., $R_S = Q$, and considering that R_1 is small in comparison with R_S , we have

$$\sigma_{MS} - \sigma_{M1} = Q \quad (16)$$

Hence, the parameter Q is obtained from the difference between the maximum stresses of the stable and first cycle. Figure 5(a) for the case $\Delta \varepsilon = 2.2\%$ yields this difference as

$$Q = 47 \text{ MPa} \quad (17)$$

²As discussed in Appendix A, the first and second back stresses level to C_i/γ_i in the loading part of the curve within the strain range. Hence, we can write $(\alpha_1 + \alpha_2)_{M1} = (\alpha_1 + \alpha_2)_{MS} = C_1/\gamma_1 + C_2/\gamma_2$. Knowing that the maximum of third back stress is $C_3 \varepsilon_{\text{max}}^p$, for both first cycle and stable cycle, we can obtain $(\alpha_1 + \alpha_2 + \alpha_3)_{M1} = (\alpha_1 + \alpha_2 + \alpha_3)_{MS} = C_1/\gamma_1 + C_2/\gamma_2 + C_3 \varepsilon_{\text{max}}^p$.

Table 3 Calibrated material parameters for SM490YB steel in air and in 1 MPa H₂ gas

Parameter	Symbol	air	Hydrogen
Young's modulus	E	200 GPa	200 GPa
Initial yield stress	σ_0	220 MPa	184 MPa
Evolution of back stress	C_1	3.2×10^5 MPa	3.2×10^5 MPa
	C_2	6.8×10^4 MPa	9×10^4 MPa
	C_3	5.3×10^3 MPa	5.5×10^3 MPa
	γ_1	2×10^4	3.2×10^4
	γ_2	530	570
	γ_3	12	25
Evolution of isotropic hardening/softening parameter R	h	2	4
	Q	47 MPa	37 MPa

The values of the remaining parameters C_2 , γ_1 , γ_2 , and σ_0 are determined by simulating the experimentally measured stable hysteresis loop shown in Fig. 12 through using Eq. (9). Nonlinear least square approximation yields $C_2 = 6.8 \times 10^4$ MPa, $\gamma_1 = 2 \times 10^4$, $\gamma_2 = 530$, and $\sigma_0 = 220$ MPa; see Appendix B. The calibrated parameters are listed in Table 3. As can be seen, the magnitudes of C_2 and C_3 are, respectively, one and two orders of magnitude less than the magnitude of C_1 ; and this validates the approximation that C_1 controls the slope of the hysteresis loop at zero plastic strain. Similarly the parameters γ_1 and γ_2 are large enough so that the assumption $\exp(-\gamma_i \Delta \epsilon^p) \sim 0$ holds and C_3 controls the slope of the hysteresis loop close to ϵ_{\max}^p .

Figure 13 shows the stable hysteresis loop predicted by the model, Eq. (9), for $\epsilon_{\max}^p = -\epsilon_{\min}^p = 1\%$ along with the corresponding three back stresses, Eqs. (A7) and (A8), in the absence of hydrogen. The first back stress, α_1 , starts with a large initial slope and quickly levels to C_1/γ_1 ($-C_1/\gamma_1$) on the loading (unloading) part of the curve. We note again that the first back stress underpins the segment 1 in Fig. 13. Similarly, the second back stress levels to C_2/γ_2 ($-C_2/\gamma_2$) on the loading (unloading) part of the curve and underpins the segment 2 in Fig. 13, which is the nonlinear portion of the stable hysteresis curve. The third back stress starts from $C_3 \epsilon_{\min}^p$ ($C_3 \epsilon_{\max}^p$) on the

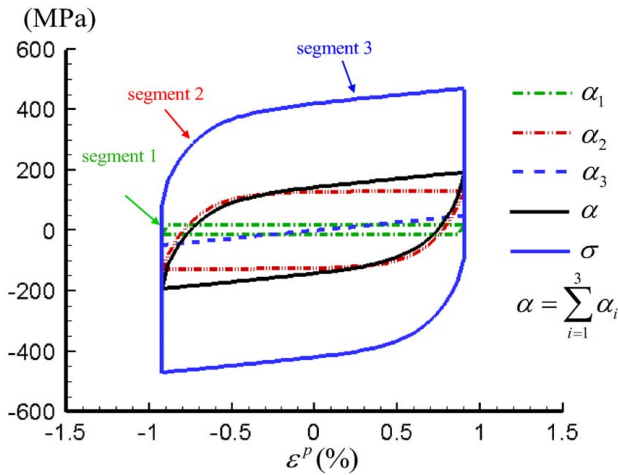


Fig. 13 Model prediction of the stable stress–strain hysteresis loop along with the associated back stress α for uniaxial strain-controlled cyclic loading with strain range 2.2% in the absence of hydrogen. The calibrated model parameters are listed in Table 3.

loading (unloading) part and passes through the origin. The third back stress underpins the segment 3 in Fig. 13 which is the linear part of the stable hysteresis curve at large plastic strains.

Interestingly, the calibrated parameters provide fairly good agreement between the model and the experimental data for the hysteresis loop at stabilization also for strain ranges $\Delta \epsilon = 1.08\%$ and 0.92% , as shown in Fig. 14. The agreement is remarkable if one considers that the experimental data from these two tests were not used in the calibration process.

4.2 Determination of Parameters $C_1, C_2, C_3, \gamma_1, \gamma_2, Q$, and σ_0 in the Presence of Hydrogen. For the calibration in the presence of hydrogen, we used the experimental data from the stable hysteresis loops shown in Fig. 15 for strain range $\Delta \epsilon = 2.2\%$ in 1 MPa hydrogen gas environment and room temperature. Following the same calibration procedure detailed in Sec. 4.1, we determined $C_1, C_2, C_3, \gamma_1, \gamma_2, Q$, and σ_0 ; results are shown in Table 3. The calibrated model predictions are shown as continuous lines superposed on Fig. 15. Remarkably, the model also reproduces the experimental data for $\Delta \epsilon = 1.08\%$ and 0.92% fairly well.

4.3 Determination of the Parameter h in the Absence and Presence of Hydrogen. According to Eq. (8), the parameter h controls the rate of cyclic hardening, that is, how fast the maximum stress in each cycle changes toward the maximum stress in the stabilized cycle. A smaller h is associated with a larger number of cycles till stabilization, which also implies that the number of cycles for the isotropic hardening (softening) parameter R to increase (decrease) from zero to Q is larger.

Given that $\alpha_{M1} = \alpha_{MN}$, Eq. (14) yields for the maximum stresses σ_{M1} and σ_{MN} , respectively, for the 1st and N^{th} cycles at $\epsilon^p = \epsilon_{\max}^p$:

$$\sigma_{MN} - \sigma_{M1} = R_N - R_1 \quad (18)$$

where R_N is the value of the parameter R associated with cycle N . With R_1 being small in comparison with R_N , we find

$$\sigma_{MN} - \sigma_{M1} = R_N \quad (19)$$

Combining Eqs. (16) and (19) yields

$$\frac{\sigma_{MN} - \sigma_{M1}}{\sigma_{MS} - \sigma_{M1}} = \frac{R_N}{Q} \quad (20)$$

Given that $\Delta \epsilon^p$ is the plastic range of a cycle, the total accumulated plastic strain in cycle N is $\epsilon^p = 2N\Delta \epsilon^p$ and Eq. (8) gives

$$R_N = Q(1 - e^{-h(2N\Delta \epsilon^p)}) \quad (21)$$

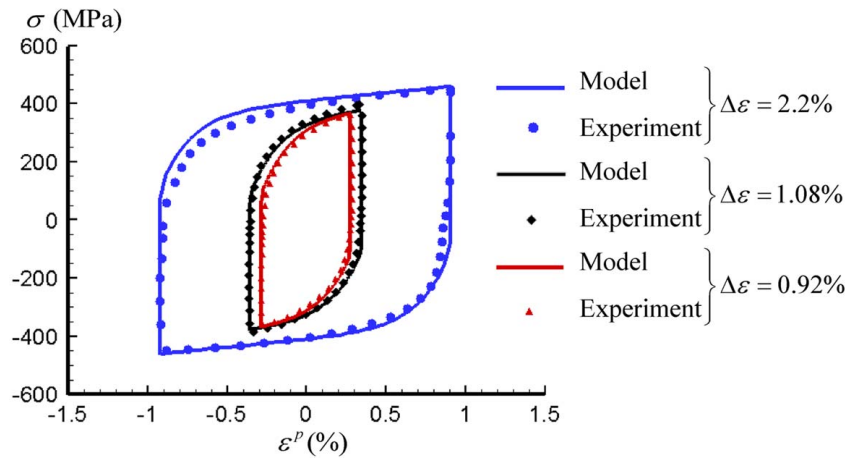


Fig. 14 Comparison of the stable hysteresis loops between the calibrated model and experimental data for uniaxial strain-controlled cyclic loading with strain range 2.2%, 1.08%, and 0.92% in the absence of hydrogen. The calibrated model parameters are listed in Table 3.

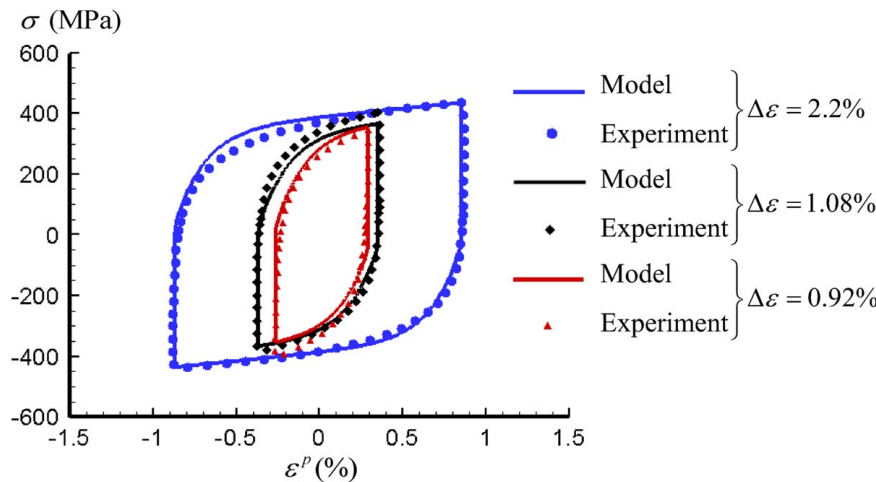


Fig. 15 Comparison of the stable hysteresis loop predictions by the calibrated model with experimental data for uniaxial strain-controlled cyclic loading with strain range 2.2%, 1.08%, and 0.92% in the presence of hydrogen. The calibrated model parameters are listed in Table 3.

Substitution of Eq. (21) in Eq. (20) provides

$$\frac{\sigma_{MN} - \sigma_{M1}}{\sigma_{MS} - \sigma_{M1}} = 1 - e^{-h(2N\Delta\epsilon^p)} \quad (22)$$

The parameter h is calculated by using Eq. (22) to fit the experimental data for the normalized maximum stress difference $(\sigma_{MN} - \sigma_{M1})/(\sigma_{MS} - \sigma_{M1})$ as a function of accumulated plastic strain. As shown in Fig. 16, a fairly good fitting of the experimental data for $\Delta\epsilon = 2.2\%$ is obtained with $h=2$ and $h=4$ for the uncharged and hydrogen-charged specimens, respectively.

4.4 Determination of the Parameter γ_3 in the Absence and Presence of Hydrogen. The remaining parameter γ_3 is determined by using the ratcheting data shown in Fig. 10 obtained from uniaxial stress-controlled cyclic loading tests with stress amplitude $\sigma_a = 420$ MPa at mean stress $\sigma_{\text{mean}} = 20$ and 40 MPa. As shown in Fig. 10, immediately upon yielding, a long elongation was found which is behavior associated with rapid onset of Lüders bands. We corrected for this elongation by subtracting the maximum strain of the first cycle, $\epsilon_{\text{max}|N=1}$, from the ratcheting data for

all other cycles; the ratcheting strain thus calculated as $\epsilon_{\text{ratchet}} = \epsilon_{\text{max}} - \epsilon_{\text{max}|N=1}$. The data are replotted in Fig. 17.

Using the calibrated model, we carried out finite element simulations of the ratcheting tests by varying γ_3 and keeping all other parameters fixed so as to best reproduce the ratcheting response. The simulated uniaxial tension domain was loaded incrementally by changing the applied stress from $\sigma_{\text{min}} = -400$ MPa to $\sigma_{\text{max}} = 440$ MPa for mean stress $\sigma_{\text{mean}} = 20$ MPa and from $\sigma_{\text{min}} = -380$ MPa to $\sigma_{\text{max}} = 460$ MPa for $\sigma_{\text{mean}} = 40$ MPa. The finite element calculations were carried out under axisymmetric conditions and the Chaboche model as outlined in Sec. 3.1 was integrated by following Hosseini et al. [29]. The best match between simulation and experimental results was obtained when $\gamma_3 = 12$ in the absence of hydrogen and $\gamma_3 = 25$ in the presence of hydrogen. Figures 17(a) and 17(b) show the comparison between the calibrated model predictions and the experimental ratcheting data in the absence and presence of hydrogen, respectively. The agreement between model predictions and experimental data is deemed to be satisfactory. We note that the ratcheting data vary almost linearly with strain and this linearity is captured by the calibrated model. Lastly, in view of the fact that $\epsilon_{\text{max}}^p = 1.0\%$ for the cycle with 2.2% strain range we find $\gamma_3 \epsilon_{\text{max}}^p = 0.12$ and 0.25 in the absence

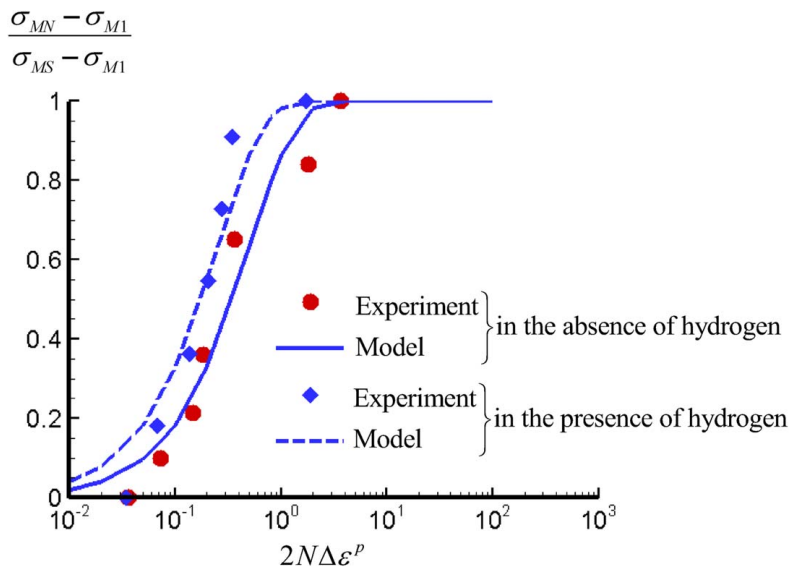


Fig. 16 Comparison of the model prediction of the normalized maximum stress difference $(\sigma_{MN} - \sigma_{M1})/(\sigma_{MS} - \sigma_{M1})$ with the experimental data for uniaxial strain-controlled cyclic loading with strain range 2.2% in the absence and presence of hydrogen. The parameters σ_{MS} , σ_{MN} , and σ_{M1} denote, respectively, the maximum stress in the stabilized cycle, cycle N , and first cycle.

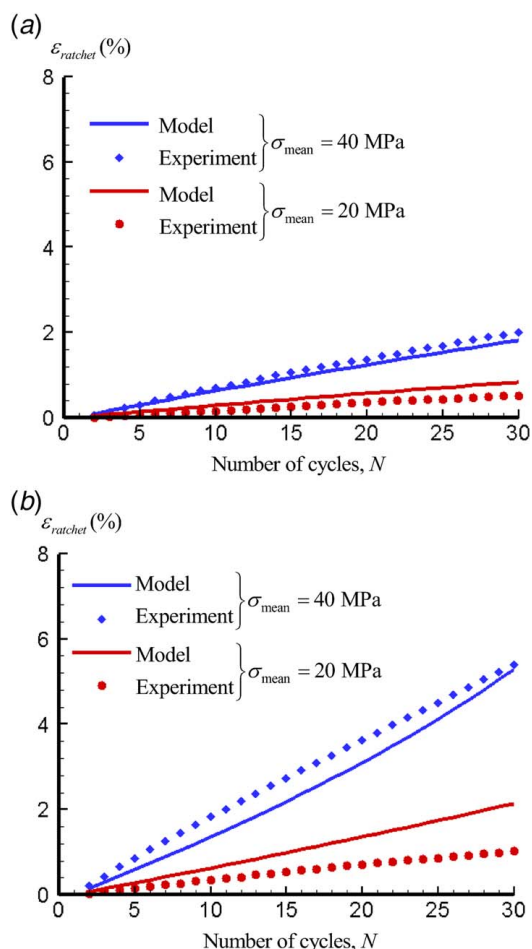


Fig. 17 Model prediction of ratcheting response with (a) $\gamma_3 = 12$ in the absence of hydrogen and (b) $\gamma_3 = 25$ in the presence of hydrogen. The experimental data were obtained with stress amplitude $\sigma_a = 420$ MPa and mean stress $\sigma_{mean} = 20$ and 40 MPa.

and presence of hydrogen, respectively. It should be remembered that $\gamma_3 \epsilon_{max}^p < 1$ is compatible with the requirement of nearly linear variation of the third hardening rule as function of the plastic strain.

5 Discussion

We investigated the effect of hydrogen on the constitutive response of the low carbon steel, SM490YB, by carrying out cycling uniaxial strain-controlled and ratcheting tests in 1.0 MPa H_2 gas at room temperature. The hysteresis loops in the absence of hydrogen show that the steel is hardened at $\Delta\epsilon = 2.2\%$ and softened at 0.92% and 1.08%. Hydrogen softened the response for all three strain ranges, although the effect is almost negligible for 0.92% and 1.08% (Figs. 6–8). On the other hand, a large hydrogen effect was observed on ratcheting as shown in Fig. 10. We

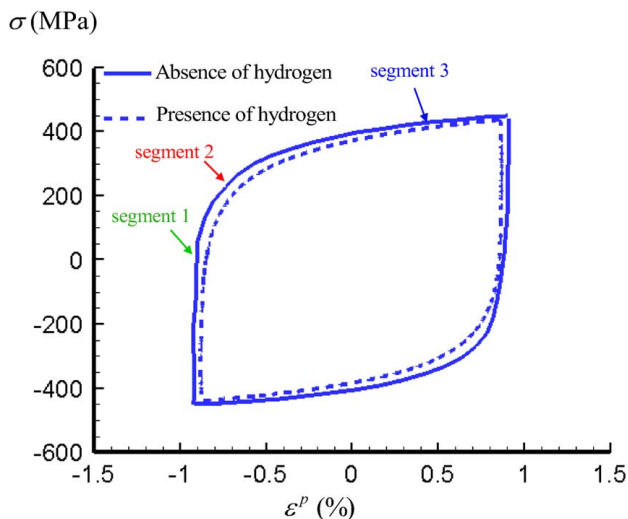


Fig. 18 Experimentally measured stable hysteresis curves in the absence and presence of hydrogen under uniaxial strain-controlled cyclic loading with strain range 2.2%

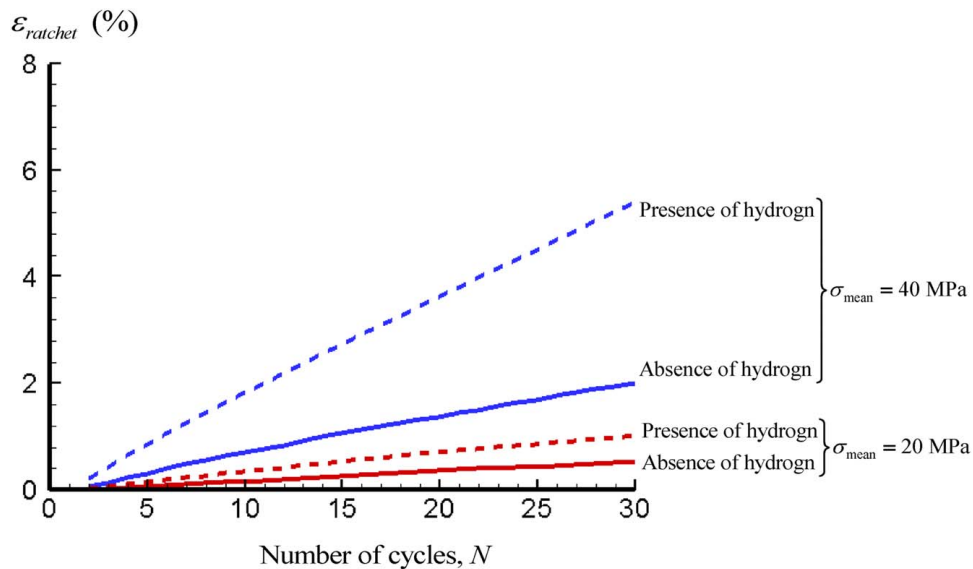


Fig. 19 Comparison between the ratcheting data in the presence and the absence of hydrogen from stress-controlled tests with stress amplitude $\sigma_a = 420$ MPa at mean stress $\sigma_{\text{mean}} = 20$ and 40 MPa

simulated the experimental response through the Chaboche model which is so constructed to capture material response in cyclic loading. The model involves nine phenomenological parameters which are identified with features of the experimentally measured response. We proposed a calibration procedure for these nine parameters, and based on the calculated values we attempted to associate the hydrogen effect with standard phenomenological descriptors such as hardening, yielding, and ratcheting.

Figure 18 shows the stable hysteresis curves for the charged and uncharged specimens from strain-controlled tests with strain range 2.2% and for which $\epsilon_{\text{min}}^p = -1\%$. The two nearly linear parts of the stable hysteresis curves at large plastic strains whose slope is controlled by the parameter C_3 , i.e., segment 3, are almost parallel to each other. Hence, the hydrogen effect on the parameter C_3 is not significant, and this is shown by the close values 5.5×10^3 and 5.3×10^3 MPa, respectively, in the presence and absence of hydrogen. Similarly, looking at segment 1, one argues that there is no hydrogen effect on the parameter C_1 . The parameter C_1 is equal to 3.2×10^5 MPa in both cases of hydrogen and no hydrogen. In summary, whereas hydrogen has a discernible effect on the parameter C_2 (slope of segment 2), and this is shown by the values 9×10^4 and 6.8×10^4 MPa, respectively, in the presence and absence of hydrogen, its effect on C_1 and C_2 is not significant. To conclude, additional experimental data for a range of hydrogen pressures are needed to understand the effect of hydrogen on the parameters C_1 , C_2 , and C_3 .

Figure 18 shows that the maximum stresses in the stable hysteresis curves are 435 MPa and 450 MPa in the presence and absence of hydrogen, respectively. From Eq. (11) along with the fact that C_1/γ_1 is small compared with C_2/γ_2 , C_2/γ_2 , and C_3 are larger in hydrogen than in air, we deduce that the lower maximum stress in the presence of hydrogen is associated with a lower yield stress σ_0 and Q . Indeed, the yield stress $\sigma_0 = 184$ MPa in the presence of hydrogen is lower than $\sigma_0 = 220$ MPa in the absence of hydrogen (see Table 3) by 16.4%. Table 3 also shows that the value of the parameter Q in the presence of hydrogen, $Q = 37$ MPa, is by 21% lower than that in the absence of hydrogen, $Q = 47$ MPa. This 21% lower value of Q in the presence of hydrogen indicates less isotropic hardening. Lastly, the calibrated values of h were 4 and 2 in the presence and absence of hydrogen, respectively. Hence, cyclic hardening in the presence of hydrogen is faster, which is associated with a smaller number of cycles to stabilization.

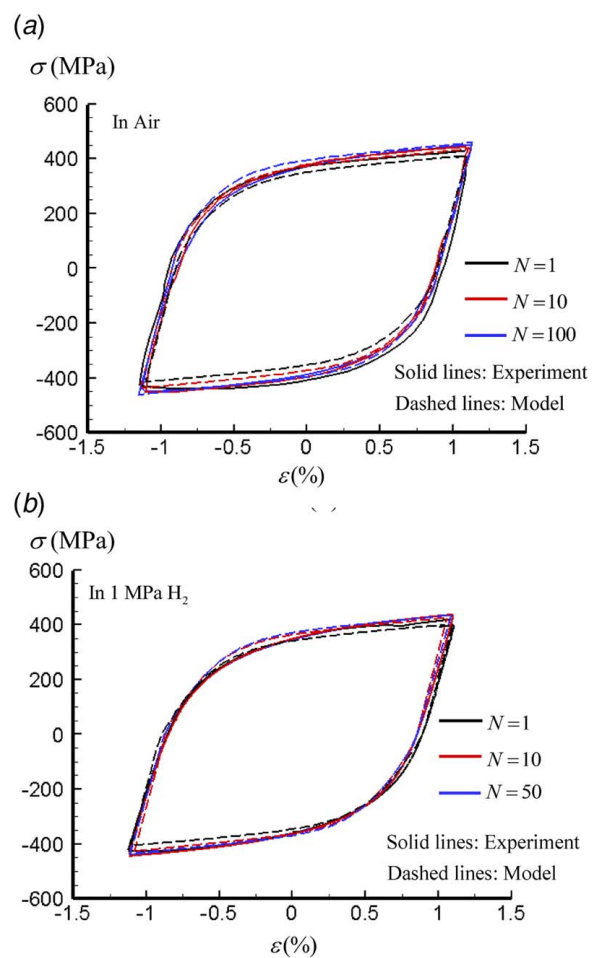


Fig. 20 Comparison of the stress–strain curves predicted by the calibrated model (dashed lines) with the experimental data (solid lines) for uniaxial strain-controlled cyclic loading with strain range 2.2%: (a) in air for cycles $N = 1, 10,$ and 100 and (b) in 1 MPa hydrogen gas for cycles $N = 1, 10,$ and 50. The calibrated model parameters are listed in Table 3.

It is worth pointing out that a marked hydrogen effect was observed on the ratcheting response of the JIS SM490YB steel. The parameter γ_3 which governs the ratcheting response is 108% larger in the presence of hydrogen, $\gamma_3 = 25$, than in the absence, $\gamma_3 = 12$. Figure 19 shows that hydrogen increases ratcheting significantly, especially at the larger mean stress 40 MPa.

Lastly, Fig. 20 shows the comparison of the model predictions with the experimental response for the transient stress–strain hysteresis loop at strain range 2.2% from the first cycle to the stabilized cycle, i.e., cycles 1, 10, and 100 in air and cycles 1, 10, and 50 in the presence of hydrogen. The agreement can be deemed as good if one considers that the experimental data for cycles 1 and 10 were not used in the model calibration process.

Before closing, we wish to point out that we observed a dependence of the cyclic hardening/softening behavior in the experimental data from strain-controlled tests on strain amplitude. The material of this study, SM490YB steel, is one with an annealed microstructure and one might have expected to cyclically harden [48] at all strain amplitudes. However, testing showed softening for strain ranges 0.92% and 1.08%, and hardening for 2.2%. Softening for the strain ranges 0.92% and 1.08% can be attributed to the continuous increase of the plastically deforming volume of material along the gauge length. However, in the test with the highest strain range, 2.2%, the entire gauge length is already plastically deformed after the first quarter of the first cycle and the subsequent development of the dislocation density and arrangement leads to cyclic hardening. This phenomenon of initial cyclic softening and subsequent hardening at higher strains is well known in low carbon steels where cyclic loading effectively removes the upper yield point and Luders' strains [49]. The latter effects are associated microscopically with the removal under cyclic loading of dislocation pinning by interstitial carbon "atmospheres," which controls the upper yield point under monotonic loads.

Finally, we note that fatigue is generally regarded as the most ubiquitous mode of failure of industrial structures and components, and similarly hydrogen provides a potent source for the degradation of the structural integrity of innumerable metals and alloys. Accordingly, hydrogen-assisted fatigue in many respects represents the perfect storm, yet despite this, theoretical models for this phenomenon are almost non-existent. To comprehend and model the role of hydrogen in fatigue, it is vital to discern the salient hydrogen-induced damage mechanisms and how these translate to the propagation of a fatigue crack under cyclic loading. The first step to achieving this understanding is to develop a model to describe cyclic plasticity, which is the principal driving force for fatigue crack advance, but specifically in the presence of hydrogen. This has been the prime objective of this work.

6 Conclusions

The description of cyclic plasticity during fatigue crack growth in the presence of hydrogen requires the development of a constitutive model that accounts for the experimentally observed hydrogen effects on material response in cyclic loading. Toward this goal, the Chaboche model was used to characterize constitutively a low carbon SM490YB in air and in 1 MPa hydrogen gas at room temperature. For the calibration of the model which involves nine parameters, uniaxial strain-controlled cyclic and ratcheting tests were used. From the combined experimental and modeling results, we deduce the following:

- This low carbon steel shows a lower yield strength in the presence of hydrogen.
- At strain amplitude 2.2%, the amount of cyclic hardening is smaller in the presence of hydrogen. This observation is related to a lower value of the parameter Q in the Chaboche model that is used to describe isotropic hardening. Similarly, cyclic hardening in the presence of hydrogen is faster than that in the absence of hydrogen, which is expressed by a higher value of the parameter h .

- Ratcheting increases in the presence of hydrogen.
- Stronger recovery was found in the presence of hydrogen. This observation is reflected in the model by the higher values of the parameters γ_1 and γ_2 in the presence of hydrogen.
- The parameters C_1 and C_3 in the presence of hydrogen are almost the same as those in the absence of hydrogen, whereas the parameter C_2 is higher in the presence of hydrogen. Additional experimental data are needed to understand the effect of hydrogen as described by the three kinematic hardening rules of the model.

In summary, the objective of this study was to demonstrate the principle of how a constitutive model can be developed based on experimental data in two environments (air and hydrogen). When such a constitutive model is then applied to simulate fatigue crack growth, then there must be more comprehensive data to ensure the accuracy of the constitutive model parameters. Based on the experimental data and the trends teased out from the calibrated Chaboche model, we may conclude that hydrogen decreases the yield strength and the amount of cyclic hardening. On the other hand, hydrogen increases ratcheting, the rate of cyclic hardening, and promotes stronger recovery.

Acknowledgment

The authors gratefully acknowledge the support of the International Institute for Carbon Neutral Energy Research (WPI-I2CNER), sponsored by the World Premier International Research Center Initiative (WPI), MEXT, Japan.

Conflict of Interest

There are no conflicts of interest.

Data Availability Statement

The datasets generated and supporting the findings of this article are obtainable from the corresponding author upon reasonable request. The authors attest that all data for this study are included in the paper.

Appendix A

Uniaxial Cyclic Response of a Material Characterized by the Chaboche Constitutive Model. To demonstrate the features associated with the Chaboche model with three kinematic hardening rules, we consider the uniaxial strain-controlled response under fully reversed cyclic loading, i.e., $\epsilon_{\max}^p = -\epsilon_{\min}^p$. The only nonzero stress component is the axial stress σ_{xx} and the matrix of the back stress tensor is

$$[\alpha] = \begin{bmatrix} \alpha_{xx} & 0 & 0 \\ 0 & -\alpha_{xx}/2 & 0 \\ 0 & 0 & -\alpha_{xx}/2 \end{bmatrix} \quad (\text{A1})$$

where α_{xx} is the normal component in the loading direction x . The component α_{xx} is composed of three parts: $\alpha_{xx} = (\alpha_{xx})_1 + (\alpha_{xx})_2 + (\alpha_{xx})_3$ in which $(\alpha_{xx})_i$ is the normal component of the i th back stress in the loading direction. The yielding condition as given by Eq. (3) reduces to

$$f = \lambda \left(\sigma_{xx} - \frac{3}{2} \alpha_{xx} \right) - \sigma_0 - R = 0 \quad (\text{A2})$$

where λ is the loading/unloading parameter such that $\lambda = 1$ for loading and $\lambda = -1$ for unloading. Setting $\alpha_i = 3(\alpha_{xx})_i/2$, we set $3\alpha_{xx}/2 = \alpha_1 + \alpha_2 + \alpha_3 = \alpha$. Then, Eqs. (A2) and (4) reduce,

respectively, to

$$f = \lambda \sigma_{xx} - \lambda \alpha - \sigma_0 - R = 0 \quad (\text{A3})$$

and

$$\alpha_i = C_i \varepsilon^p - \lambda \gamma_i \alpha_i \varepsilon^p. \quad i = 1, 2, 3 \quad (\text{no summation over } i) \quad (\text{A4})$$

Solving Eq. (A4) for the first and second back stress yields

$$\alpha_i = \lambda \frac{C_i}{\gamma_i} + \left(\alpha_{i0} - \lambda \frac{C_i}{\gamma_i} \right) \exp(-\lambda \gamma_i (\varepsilon^p - \varepsilon_0^p)), \quad i = 1, 2 \quad (\text{A5})$$

where α_{i0} and ε_0^p are the values of α_i and ε^p at the start of loading or unloading. We also note that

$$\alpha_{i0} = \begin{cases} -\frac{C_i}{\gamma_i}, & \varepsilon_0^p = \varepsilon_{\min}^p \quad i = 1, 2 \quad \text{for the loading part} \\ +\frac{C_i}{\gamma_i}, & \varepsilon_0^p = \varepsilon_{\max}^p \quad i = 1, 2 \quad \text{for the unloading part} \end{cases} \quad (\text{A6})$$

From Eqs. (A5) and (A6), we find

$$\alpha_i = \lambda \frac{C_i}{\gamma_i} (1 - 2 \exp(-\lambda \gamma_i (\varepsilon^p - \lambda \varepsilon_{\min}^p))), \quad i = 1, 2 \quad (\text{A7})$$

(no summation over i)

The first and second back stresses, α_i , have an initial slope $2C_i$ at ε_{\min}^p and level, respectively, to C_i/γ_i with increasing plastic strain, provided that the parameters γ_i are large so that $\exp(-\lambda \gamma_i \Delta \varepsilon^p) \sim 0$.

The linearity of segment 3 (Fig. 12), which is controlled by the third hardening rule and which should pass through the origin due to the symmetry of the hysteresis loop, is enforced by taking γ_3 to be such that $\gamma_3 \varepsilon_{\max}^p$ is less than unity. In this case, integration of Eq. (A4) for the third hardening rule ($i = 3$) yields

$$\alpha_3 \approx C_3 \varepsilon^p \quad (\text{A8})$$

Given that R levels to Q at stabilization, substitution of Eqs. (A8) and (A7) in Eq. (A3) provides the closed form solution for the stable hysteresis loop as

$$\begin{aligned} \sigma_{xx} &= \alpha_1 + \alpha_2 + \alpha_3 + \lambda \sigma_0 + \lambda Q \\ &= \frac{C_1}{\gamma_1} (1 - 2 \exp(-\lambda \gamma_1 (\varepsilon^p - \lambda \varepsilon_{\min}^p))) \\ &\quad + \frac{C_2}{\gamma_2} (1 - 2 \exp(-\lambda \gamma_2 (\varepsilon^p - \lambda \varepsilon_{\min}^p))) + C_3 \varepsilon^p + \lambda \sigma_0 + \lambda Q \end{aligned} \quad (\text{A9})$$

Appendix B

On the Calibration of the Chaboche Model Parameters C_2, γ_1, γ_2 , and σ_0 . As presented in Sec. 3, Chaboche's constitutive model for cyclic plasticity involves nine parameters, $C_1, C_2, C_3, \gamma_1, \gamma_2, \gamma_3, Q, h$, and σ_0 , that need to be calibrated through experiment. The details of the determination of the parameters C_1, C_3, γ_3, Q , and h through using the hysteresis loop from the uniaxial strain-controlled cyclic test are given in Sec. 4. In this appendix, we describe the calibration of the parameters C_2, γ_1, γ_2 , and σ_0 .

The closed form solution for uniaxial strain-controlled cyclic loading was found in Sec. 3.2 as

$$\begin{aligned} \sigma_{xx} &= \frac{C_1}{\gamma_1} (1 - 2 \exp(-\lambda \gamma_1 (\varepsilon^p - \lambda \varepsilon_{\min}^p))) \\ &\quad + \frac{C_2}{\gamma_2} (1 - 2 \exp(-\lambda \gamma_2 (\varepsilon^p - \lambda \varepsilon_{\min}^p))) + C_3 \varepsilon^p + \lambda \sigma_0 + \lambda Q \end{aligned} \quad (\text{B1})$$

where λ is the loading/unloading parameter such that $\lambda = 1$ for loading and $\lambda = -1$ for unloading. In this equation, the parameters C_1, C_3 , and Q are already known from the calibration process discussed in Sec. 4.1. For the calibration of the parameters

C_2, γ_1, γ_2 , and σ_0 , we used least squares optimization along with Eq. (B1) as follows:

- (i) From the stable stress-strain hysteresis loop data obtained from the uniaxial strain-controlled cyclic loading test, we considered a series of n stress-strain data $(\sigma_i^{\text{exp}}, \varepsilon_i^p)$.
- (ii) For a given strain ε_i^p , Eq. (B1) provides the model prediction σ_i^{model} . The difference between the model prediction, σ_i^{model} , and the experimentally measured stress, σ_i^{exp} , is the error of the calibrated model prediction. Using the MATLAB optimization toolbox with $n = 100$, we obtained the parameters C_2, γ_1, γ_2 , and σ_0 by minimizing the sum of the squared errors

$$SSE = \sum_{i=1}^n (\sigma_i^{\text{exp}}(\varepsilon_i^p) - \sigma_i^{\text{model}}(\varepsilon_i^p))^2 \quad (\text{B2})$$

References

- [1] Suresh, S., and Ritchie, R. O., 1982, "Mechanistic Dissimilarities Between Environmentally Influenced Fatigue-Crack Propagation at Near-Threshold and Higher Growth Rates in Lower Strength Steels," *Met. Sci.*, **16**(11), pp. 529–538.
- [2] Kameda, J., and McMahon, C. J. J., 1983, "Solute Segregation and Hydrogen-Induced Intergranular Fracture in an Alloy Steel," *Metall. Trans. A, Phys. Metall. Mater. Sci.*, **14A**(4), pp. 903–911.
- [3] Wang, S., Nagao, A., Sofronis, P., and Robertson, I. M., 2019, "Assessment of the Impact of Hydrogen on the Stress Developed Ahead of a Fatigue Crack," *Acta Mater.*, **174**, pp. 181–188.
- [4] Wang, S., Nygren, K. E., Nagao, A., Sofronis, P., and Robertson, I. M., 2019, "On the Failure of Surface Damage to Assess the Hydrogen-Enhanced Deformation Ahead of Crack Tip in a Cyclically Loaded Austenitic Stainless Steel," *Scr. Mater.*, **166**, pp. 102–106.
- [5] San Marchi, C., Somerday, B. P., Nibur, K. A., Stalheim, D. G., Boggess, T., and Jansto, S., 2010, "Fracture and Fatigue of Commercial Grade Api Pipeline Steels in Gaseous Hydrogen," *American Society of Mechanical Engineers, Pressure Vessels and Piping Division PVP*, ASME Press, Bellevue, WA, pp. 939–948, PVP2010-25825.
- [6] Nibur, K. A., San Marchi, C., and Somerday, B. P., 2010, "Fracture and Fatigue Tolerant Steel Pressure Vessels for Gaseous Hydrogen," *American Society of Mechanical Engineers, Pressure Vessels and Piping Division PVP*, ASME Press, Bellevue, WA, pp. 1–10, PVP2010-25827.
- [7] San Marchi, C., Somerday, B. P., Nibur, K. A., Stalheim, D. G., Boggess, T., and Jansto, S., 2011, "Fracture Resistance and Fatigue Crack Growth of X80 Pipeline Steel in Gaseous Hydrogen," *American Society of Mechanical Engineers, Pressure Vessels and Piping Division PVP*, ASME Press, Baltimore, MA, pp. 841–849, PVP2011-57684.
- [8] Nagao, A., Hayashi, K., Oi, K., and Mitao, S., 2012, "Effect of Uniform Distribution of Fine Cementite on Hydrogen Embrittlement of Low Carbon Martensitic Steel Plates," *ISIJ Int.*, **52**(2), pp. 213–221.
- [9] Briottet, L., Moro, I., and Lemoine, P., 2012, "Quantifying the Hydrogen Embrittlement of Pipeline Steels for Safety Considerations," *Int. J. Hydrogen Energy*, **37**(22), pp. 17616–17623.
- [10] Michler, T., Naumann, J., Weber, S., Martin, M., and Pargerter, R., 2013, "S-N Fatigue Properties of a Stable High-Aluminum Austenitic Stainless Steel for Hydrogen Applications," *Int. J. Hydrogen Energy*, **38**(23), pp. 9935–9941.
- [11] Somerday, B. P., Sofronis, P., Nibur, K. A., San Marchi, C., and Kirchheim, R., 2013, "Elucidating the Variables Affecting Accelerated Fatigue Crack Growth of Steels in Hydrogen Gas With Low Oxygen Concentrations," *Acta Mater.*, **61**(16), pp. 6153–6170.
- [12] Shinko, T., Hénaff, G., Halm, D., Benoit, G., Bilotta, G., and Arzaghi, M., 2019, "Hydrogen-Affected Fatigue Crack Propagation at Various Loading Frequencies and Gaseous Hydrogen Pressures in Commercially Pure Iron," *Int. J. Fatigue*, **121**, pp. 197–207.
- [13] Sofronis, P., and McMeeking, R. M., 1989, "Numerical Analysis of Hydrogen Transport Near a Blunting Crack Tip," *J. Mech. Phys. Solids*, **37**(3), pp. 317–350.
- [14] Sofronis, P., Liang, Y., and Aravas, N., 2001, "Hydrogen Induced Shear Localization of the Plastic Flow in Metals and Alloys," *Eur. J. Mech. A/Solids*, **20**(6), pp. 857–872.
- [15] Martin, M. L., Somerday, B. P., Ritchie, R. O., Sofronis, P., and Robertson, I. M., 2012, "Hydrogen-Induced Intergranular Failure in Nickel Revisited," *Acta Mater.*, **60**(6–7), pp. 2739–2745.
- [16] Dadfarnia, M., Martin, M. L., Nagao, A., Sofronis, P., and Robertson, I. M., 2015, "Modeling Hydrogen Transport by Dislocations," *J. Mech. Phys. Solids*, **78**, pp. 511–525.
- [17] Robertson, I. M., Sofronis, P., Nagao, A., Martin, M. L., Wang, S., Gross, D. W., and Nygren, K. E., 2015, "Hydrogen Embrittlement Understood," *Metall. Mater. Trans. A*, **46**(6), pp. 2323–2341.
- [18] Martin, M. L., Dadfarnia, M., Nagao, A., Wang, S., and Sofronis, P., 2019, "Enumeration of the Hydrogen-Enhanced Localized Plasticity Mechanism for Hydrogen Embrittlement in Structural Materials," *Acta Mater.*, **165**, pp. 734–750.
- [19] Nagao, A., Dadfarnia, M., Somerday, B. P., Sofronis, P., and Ritchie, R. O., 2018, "Hydrogen-Enhanced-Plasticity Mediated Decohesion for Hydrogen-Induced Intergranular and 'Quasi-Cleavage' Fracture of Lath Martensitic Steels," *J. Mech. Phys. Solids*, **112**, pp. 403–430.

- [20] Cialone, H. J., and Holbrook, J. H., 1988, "Sensitivity of Steels to Degradation in Gaseous Hydrogen," *Hydrogen Embrittlement: Prevention and Control*, ASTM STP 962, L. Raymond, ed., American Society for Testing and Materials, Philadelphia, PA, pp. 134–152.
- [21] Hosseini, Z. S., Dadfarnia, M., Nibur, K. A., Somerday, B. P., Gangloff, R. P., and Sofronis, P., 2017, "Trapping Against Hydrogen Embrittlement," *Proceeding of the 2016 Hydrogen Conference, Material Performance in Hydrogen Environment*, B. P. Somerday, and P. Sofronis, eds., ASME Press, New York, pp. 71–80.
- [22] Uyama, H., Nakashima, M., Morishige, K., Mine, Y., and Murakami, Y., 2006, "Effects of Hydrogen Charge on Microscopic Fatigue Behaviour of Annealed Carbon Steels," *Fatigue Fract. Eng. Mater. Struct.*, **29**(12), pp. 1066–1074.
- [23] Tsuchida, Y., Watanabe, T., Kato, T., and Seto, T., 2010, "Effect of Hydrogen Absorption on Strain-Induced Low-Cycle Fatigue of Low Carbon Steel," *Procedia Eng.*, **2**(1), pp. 555–561.
- [24] Schauer, G., Roetting, J., Hahn, M., Schreijaeig, S., Bacher-Höchst, M., and Weihe, S., 2015, "Influence of Gaseous Hydrogen on Fatigue Behavior of Ferritic Stainless Steel—A Fatigue-Life Estimation," *Procedia Eng.*, **133**, pp. 362–378.
- [25] Martin, M. L., Looney, C., Bradley, P., Lauria, D., Amaro, R., and Slifka, A. J., 2019, "Unification of Hydrogen-Enhanced Damage Understanding Through Strain-Life Experiments for Modeling," *Eng. Fract. Mech.*, **216**, p. 106504.
- [26] Das, B., and Singh, A., 2020, "Influence of Hydrogen on the Low Cycle Fatigue Performance of P91 Steel," *Int. J. Hydrogen Energy*, **45**(11), pp. 7151–7168.
- [27] Mansilla, G., Hereñú, S., and Brandaleze, E., 2014, "Hydrogen Effects on Low Cycle Fatigue of High Strength Steels," *Mater. Sci. Technol.*, **30**(4), pp. 501–505.
- [28] Morrow, J., 1965, "Cyclic Plastic Strain Energy in Fatigue of Metals," *Internal Friction, Damping, and Cyclic Plasticity*, ASTM STP 378, B. Lazan, ed., American Society for Testing and Materials, West Conshohocken, PA, pp. 45–87.
- [29] Hosseini, Z. S., Dadfarnia, M., Somerday, B. P., Sofronis, P., and Ritchie, R. O., 2018, "On the Theoretical Modeling of Fatigue Crack Growth," *J. Mech. Phys. Solids*, **121**, pp. 341–362.
- [30] Drucker, D. C., and Rice, J. R., 1970, "Plastic Deformation in Brittle Ductile Fracture," *Eng. Fract. Mech.*, **1**(4), pp. 577–602.
- [31] Jhansale, H. R., 1975, "A New Parameter for the Hysteretic Stress-Strain Behaviour of Metals," *ASME J. Eng. Mater. Technol.*, **97**(1), pp. 33–38.
- [32] Chaboche, J. L., and Nouailhas, D., 1989, "Constitutive Modeling of Ratchetting Effects Part I: Experimental Facts And Properties of The Classical Models," *ASME J. Eng. Mater. Technol.*, **111**(4), pp. 384–392.
- [33] Chaboche, J. L., and Nouailhas, D., 1989, "Constitutive Modeling of Ratchetting Effects-Part II: Possibilities of Some Additional Kinematic Rules," *ASME J. Eng. Mater. Technol.*, **111**(4), pp. 409–416.
- [34] Armstrong, P. J., and Frederick, C. O., 1966, "A Mathematical Representation of the Multiaxial Bauscinger Effect," CEBG Rep. No. RD/B/N 731.
- [35] Chaboche, J. L., Van, K. D., and Cordier, G., 1979, "Modelization of the Strain Memory Effect on the Cyclic Hardening of 316 Stainless Steel," *Transactions of the International Conference on Structural Mechanics in Reactor Technology*, Division L, Berlin, Aug. 9–21, p. L11/3.
- [36] Chaboche, J. L., 1986, "Time-Independent Constitutive Theories for Cyclic Plasticity," *Int. J. Plast.*, **2**(2), pp. 149–188.
- [37] Bower, A. F., 1989, "Cyclic Hardening Properties of Hard-Drawn Copper and Rail Steel," *J. Mech. Phys. Solids*, **37**(4), pp. 455–470.
- [38] Chaboche, J. L., 1991, "On Some Modifications of Kinematic Hardening to Improve the Description of Ratchetting Effects," *Int. J. Plast.*, **7**(7), pp. 661–678.
- [39] Ohno, N., and Wang, J. D., 1991, "Nonlinear Kinematic Hardening Rule: Proposition and Application to Ratchetting Problems," *Transactions of the 11th International Conference on Structural Mechanics in Reactor Technology*, Tokyo, Japan, Aug. 18–23, pp. 481–486.
- [40] Ohno, N., and Wang, J. D., 1993, "Kinematic Hardening Rules with Critical State of Dynamic Recovery, Part I: Formulation and Basic Features for Ratchetting Behavior," *Int. J. Plast.*, **9**(3), pp. 375–390.
- [41] Bari, S., and Hassan, T., 2000, "Anatomy of Coupled Constitutive Models for Ratchetting Simulation," *Int. J. Plast.*, **16**(3), pp. 381–409.
- [42] Nagao, A., 2019, "Experimental and Simulation Study of Hydrogen Uptake in Low-Alloy Steels Exposed to High-Pressure H₂ Gas," *Hydrogenius, I2CNER, and HydroMate Joint Research Symposium*, Fukuoka, Japan, Jan. 30, pp. 61–72.
- [43] Tsong-Pyng, P., and Altstetter, C. J., 1986, "Effects of Deformation on Hydrogen Permeation in Austenitic Stainless Steels," *Acta Metall.*, **34**(9), pp. 1771–1781.
- [44] Crank, J., 1975, *The Mathematics of Diffusion*, Oxford University Press, Bristol, UK.
- [45] Ramunni, V. P., Coelho, T. D. P., and de Miranda, P. E. V., 2006, "Interaction of Hydrogen With the Microstructure of Low-Carbon Steel," *Mater. Sci. Eng. A*, **435–436**, pp. 504–514.
- [46] Takai, K., and Watanuki, R., 2003, "Hydrogen in Trapping States Innocuous to Environmental Degradation of High-Strength Steels," *Iron Steel Inst. Japan*, **43**(4), pp. 520–526.
- [47] Lee, E. H., 1981, "Some Comments on Elastic-Plastic Analysis," *Int. J. Solids Struct.*, **17**(9), pp. 859–872.
- [48] Kang, G., and Liu, Y., 2008, "Uniaxial Ratchetting and Low-Cycle Fatigue Failure of the Steel With Cyclic Stabilizing or Softening Feature," *Mater. Sci. Eng. A*, **472**(1–2), pp. 258–268.
- [49] Gorash, Y., and Mackenzie, D., 2017, "On Cyclic Yield Strength in Definition of Limits for Characterisation of Fatigue and Creep Behaviour," *Open Eng.*, **7**(1), pp. 126–140.